sustainability

MDPI

Article

Optimizing Solar Potential Analysis in Cuba: A Methodology for High-Resolution Regional Mapping

Javier Domínguez [1,*], Carlo Bellini [2], Ana María Martín [1] and Luis F. Zarzalejo [1,*]

[1] Renewable Energies Division, Centre for Energy, Environmental and Technological Research (CIEMAT), 28040 Madrid, Spain; anamaria.martin@ciemat.es
[2] Department of Industrial Engineering, University of Padova, 35131 Padova, Italy; carlo.bellini94@gmail.com
* Correspondence: javier.dominguez@ciemat.es (J.D.) and lf.zarzalejo@ciemat.es (L.F.Z.)

Abstract: The development of solar energy at a regional scale necessitates a thorough understanding of available resources. Cuba, facing prolonged economic, environmental, and energy crises, urgently needs to enhance its sustainability through solar energy. Although solar resource mapping is widespread, Cuba lacks extensive field measurements, often relying on models that may not be ideally suited for large regions, like Matanzas province. Spanning over 12,000 km² with nearly 150 km between its northern and southern extremes, Matanzas presents challenges for high-resolution solar mapping. This study introduces a methodology that integrates various methods and databases to achieve the maximum resolution in the resulting solar map. This approach is designed for large areas, where conventional high-resolution models fall short. By optimizing calculation times and parameterizing the entire surface latitudinally, a high-resolution solar resource map for Matanzas has been developed. This map significantly enhances the understanding of solar resources in Cuba and enables the proposal of new methodologies for analyzing solar potential in similarly large regions.

Keywords: solar mapping; GIS; solar resources; solar radiation; renewable energies; rural electrification; sustainable development; high-resolution models

Citation: Domínguez, J.; Bellini, C.; Martín, A.M.; Zarzalejo, L.F. Optimizing Solar Potential Analysis in Cuba: A Methodology for High-Resolution Regional Mapping. *Sustainability* **2024**, *16*, 7899. https://doi.org/10.3390/su16187899

Academic Editors: Manuel Alcázar Ortega and Lina Montuori

Received: 19 August 2024
Revised: 5 September 2024
Accepted: 5 September 2024
Published: 10 September 2024

1. Introduction

Access to electricity is an essential requirement for human development. It is recognized as a basic need to ensure the respect of human rights and the improvement of the life quality. Despite this, there are still more than 700 million people in the world without access to electricity. Unfortunately, the COVID-19 pandemic has contributed to worsening these conditions. The International Energy Agency (IEA) estimates that in 2030, under the so-called STEPS scenario, some 670 million people worldwide will still be without access to electricity [1].

This highlights the pressing need to advance energy access strategies, with decentralized solutions emerging as one of the most effective and economical options. Renewable energies are crucial in addressing this challenge while ensuring sustainability. In many regions, they are also the most cost-effective choice. A key advantage of renewable energy is its global availability, even in areas where conventional energy distribution is challenging. However, its inherent variability—both temporal and spatial—can pose challenges for maintaining a reliable power supply. Therefore, a thorough assessment of the available energy mix is essential in the early stages of any electrification project. This process involves several factors, many of which are often identifiable at the local level.

In dealing with renewable energy sources (RESs), an adequate assessment is fundamental when working with coupling the energy demand with the power supply. Spatial and temporal variabilities play crucial roles in this process. In addition, the integration of a technology always has an important territorial impact, which is not easily detected using a merely technical approach. Geographic information systems (GISs) represent instruments

capable for integrating non-spatial features (technological, economical, etc.) into a local reality, intended not only from a geographical point of view but also from the perspective of a network of mutually related activities [2]. In short, the wide geographical dispersion that characterizes RESs and the importance for evaluating their integration at a local level fit perfectly with the potential of GIS analysis.

This study focuses on the development of solar maps aimed at enhancing rural electrification, providing decision-making tools based on GISs. These tools are designed to facilitate the integration of solar energy as a feasible strategy to address energy access challenges while enhancing the sustainable use of local resources and supporting rural populations. The primary objective of this research is to improve the resolution of solar maps using standard methodologies. To achieve this, a case study was conducted in the Matanzas province of Cuba as a part of the HIBRI2 project (Integrated Control System for Energy Supply through Hybrid Systems in Isolated Communities in Cuba, Phase II) [3,4]. This research aims to contribute to the promotion of efficient renewable energy use and development in Cuba by designing and implementing innovative systems that hybridize various technologies.

There is a wide variety of studies that highlight the value of different geographic information tools in the development of solar maps. For example, a recent work by Benalcazar [5] proposes a GIS approach that combines land eligibility and technoeconomic assessments for utility-scale photovoltaic systems. At another scale, with a focus on islands, Gacu [6] develops a solar power suitability map for establishing solar PV systems, maximizing the full potential of their land. Other authors, such as Ibraheem [7], focused their research on tools and remote-sensing data provided by governmental agencies, such as the National Aeronautics and Space Administration (NASA), and include information about direct normal irradiance (DNI) and global horizontal irradiance (GHI) data. For these data, a GIS program was used to analyze solar irradiation, digital elevation model (DEM), and land use information. This helped to identify areas suitable for solar power by considering land use and topography.

In this regard, a key work is that by Kanters [8], which raises the importance of solar maps, with a focus on an urban environment. In the case of Kanters and Loquias [8,9], implementation takes place in the Philippines, using GHI data in a raster format with 250 m of spatial resolution and a DEM of 30 m, far from the resolution required by our research. Other authors, such as Szabó [10], use existing solar maps in a raster format as a basis for a feasibility analysis at a national scale. Obviously, this requires the prior existence of such a source of information at a scale suitable for the purpose of the analysis, which is not the case herein.

Authors such as Alrawashdeh emphasize the importance of solar radiation data in the design and development of solar energy projects [11]. Alrawashdeh's study, conducted at a national scale, provides valuable insights for policymakers; however, the resolution of the data may not be suitable for local-scale applications. In a similar geographical context, Settou [12] and Hasan's [13] research focuses on the site selection for a specific solar PV power plant, utilizing high-resolution spatial data to optimize the process. Also, in Algeria, Yaiche [14] underscores the critical role of sunshine duration in solar energy assessments. In contrast, the work of Enjavi-Arsanjani [15] shifts the focus to electricity generation through concentrated solar power (CSP) in environments similar to those in previous studies, such as in Iran.

Jung [16], on the other hand, highlights the benefits for using publicly available data sources and prioritizing land with minimal competition for use in solar energy projects. The accessibility of such data is crucial for their effective application. Lastly, in the context of urban solar mapping, authors like Kanters [17] and Wegertseder [18] stress the importance for developing solar cadasters to promote solar self-consumption and optimize the urban solar potential.

Although geographic information systems, such as ArcGIS [19], are commonly used for creating solar radiation maps, they encounter difficulties when applied to large regional maps with a high metric resolution. To address this issue, a new methodology is proposed that integrates Meteonorm [20] data with ArcGIS. This approach involves tessellating the territory

into smaller units and applying Meteonorm parameters to each unit. The province of Matanzas in Cuba is selected as a case study to test this methodology, given its large size and significance for solar energy development, and it has not been previously studied at this resolution.

In dealing with solar system modeling, an input layer was required, representing the available resource. A high spatial resolution is needed because the present work is primarily designed for small-scale realities. Hence, the high-quality assessment of solar resources represents an objective of this work. The proposed approach is not limited in providing useful information for the model. A method is defined for the creation of solar radiation maps, with the purpose for being replicable for any location of interest.

2. Materials and Methods

For this study, the entire province of Matanzas (Cuba) is considered as the reference area. In order to check the results, a small area in Guasasa, at the south of the province, is used for testing. Matanzas province is located in the western region of Cuba (latitude: 23°03′4″ N and longitude: 81°34′31″ W). With an area of 11,798 km², it is the second largest province, representing 10.7% of the total area of the country. It borders the provinces of Villa Clara, Cienfuegos, and Mayabeque. This territory is characterized by the predominance of plains, which occupy three-quarters of the province, with the highest altitudes to the northwest and center west. The southern coast is, for the most part, a swampy plain. The Guasasa community (332 inhabitants) belongs to the municipality of Ciénaga de Zapata, on the southeast coast of Matanzas province. It is by the Caribbean Sea and surrounded by forests and swamps [21]. With respect to the solar potential, in the case of Cuba, the study by Prăvălie [22] highlights how most of the values are above 1800 kWh/m^2 for the annual global horizontal irradiation.

Several resources allow us to know the spatial distribution of the solar radiation over the study area. Generally, the available maps are created through the interpolation and extrapolation of data series from measurement station networks, combined with satellite estimations. Some of the most reliable and used [7,23–25] web map sources are the following:

- *Global Solar Atlas*, which is provided by the World Bank and the Energy Sector Management Assistance Program (ESMAP) and was developed by Solargis [26]. This web map offers information on global irradiation (horizontal, direct normal, and tilted optimum angles). The raster data of the average daily totals and yearly/monthly totals are available in GeoTIFF and AAIGRID formats with a spatial resolution (pixel size) of 9 arcsec (nominally, 250 m);
- *NASA PowerPrediction of Worldwide Energy Resources*, which supplies data of monthly and annual average radiations (horizontal and direct normal) under real and clear sky conditions [27]. The raster data are in ASCII, csv, GeoJSON, GeoTIFF, and NetCDF formats with a spatial resolution of 0.5 degrees. It also offers the option of data series for a single or a regional selected location;
- *Photovoltaic Geographical Information System (PVGIS)* [28] (by the European Commission), which provides a free and open-access database of solar radiation values for Europe, Africa, and most of Asia and America. The maps available for download correspond to monthly and annual global irradiances (horizontal, tilted to the optimum, and on a two-axis sun-tracking surface). The raster data are in the ESRI ascii grid format, with various spatial resolutions depending on the geographical coverage of the required database (CMSAF—0.025°, SARAH—0.05°, and NSRDB—0.04°). It also has different series of daily, monthly, and annual data for a single location.

In order to determine the radiation, data from measurement stations may also be used to generate maps through interpolating the values. Although this information may be available in yearly, monthly, and daily average series, the distribution of the stations may be uneven, and not all the regions are covered equally [29–31]. However, in dealing with small and rural areas, a more specific approach would be recommended. Isolated zones are less likely to provide direct measurements; also, topographic heterogeneity considerably affects the insolation [32]. Another option is solar radiation maps, generated with GIS software,

that model solar radiation in an area, considering the factors that influence its distribution. The set of solar radiation analysis tools in ArcGIS software, version 10.8, by ESRI, can be used to calculate the global radiation for a specific area, latitude, and time period, taking into account atmospheric conditions and the influence of the topography [33–35]. Also, the solar module *r.sun* in the GRASS GIS generates raster maps of the global radiation for a given day, considering a clear or cloudy sky environment [36–38]. This module is also integrated into the QGIS software.

This study is based on the application of the software ArcGIS, version 10.8 [19], to create a solar radiation raster map of Matanzas, with a spatial resolution of 30 m. This work first describes the operation of the *Area Solar Radiation* tool used to determine the distribution of the insolation in the geographical area [33]. Second, the input parameters required by the tool are detailed, focusing on the description of the digital elevation model (DEM), the latitude, and the determination of the parameters related to the atmospheric conditions over the years (the diffuse proportion and clarity index). These parameters are validated and the necessary corrections are proposed to adjust the results of the solar radiation. With the defined input data, we proceed to calculate the global solar radiation (monthly and annual) in the province of Matanzas. In this task, it has been necessary to divide the study area into smaller zones for the analysis and implement a Python script to run the entire process. In addition, the solar radiation is determined for a distribution of buildings at a smaller location, the community of Guasasa.

2.1. ArcGIS's Area Solar Radiation

The solar radiation distribution at the global scale is determined by latitudinal gradients due to the effects of Earth's rotation on its axis and translation around the sun. However, at the local level, topography is the main factor in the insolation distribution, affected by the altitude variation, orientation, and shadows [39].

Area Solar Radiation is an ArcGIS tool included in the *Spatial Analyst* extension. It implements a solar radiation model using a DEM as input. Its core is the viewshed algorithm, which allows us to create maps of global, direct, and diffuse radiations for a specific period of time, accounting for the site's latitude and elevation, shifts in the solar angle, atmospheric attenuation, surface orientation, and the surrounding topography. It represents an effective tool for analysis at a local scale, which may be applied in larger geographical areas, pointing out spatial and temporal variations. For this reason, *Area Solar Radiation* was chosen to create the insolation map of Matanzas.

2.1.1. Viewshed Calculation

The viewshed is the angular distribution of the sky's obstruction. For each specific position, it provides a raster representation of the visible sky and the sky direction obstructed by the surrounding topography and surface features. For each cell of the input DEM, the viewshed algorithm calculates the maximum angle of the sky's obstruction (horizon angle) for a specific set of directions around the location of interest. For all the other directions, the horizon angles are calculated using interpolation [39].

Horizon angles are then projected onto a hemispherical coordinate system. Each cell of the viewshed raster grid corresponds to both a tilt angle (β), relative to the horizontal plane, and the cell's azimuth angle (γ), relative to the south direction, allowing us to represent the three hemispherical directions as a two-dimensional grid. Once calculated and converted to the horizon angle along the set directions, the sky view associated with each cell of the DEM resembles an upward-looking fisheye photo. Such viewsheds are then overlaid with a direct sun map and a diffuse sky map to estimate the direct and diffuse radiations. Repeating the same operation for each raster cell and combining the results will produce an insolation map.

2.1.2. Sun Map and Sky Map

A sun map represents the apparent position of the sun and its variation over time. It is projected in the same hemispherical coordinates as those of the viewshed. The sun's positions, defined by the zenith (θ_z) and azimuth (Ψ), are derived through astronomical equations based on the latitude location and the specific time period [40–42]. Knowing the sun's position, the direct solar radiation can, therefore, be calculated. A time interval has to be set to define the size of the discrete sky sector that represents the sun's path. Penumbral effects are also accounted for, as are the solar disc size variations due to refraction near the horizon.

Because diffuse solar radiation is spread along any sky direction, its calculation is related to a different hemispherical raster representation. A sky map represents the entire sky divided into a series of sky sectors, which size depends on the number of divisions set for the calculation. Diffuse radiation can be calculated for each sky sector, defined by the zenith and azimuth angles of their centroid and assigned to an identifier value.

By combining the viewshed, sun map, and sky map, the unobstructed sky area is determined. Hence, the direct and diffuse solar radiations are calculated considering such area only. In particular, the proportion of the visible sky is represented by the gap fraction, calculated for each sector as the number of unobstructed cells divided by the total number of cells.

2.1.3. Solar Radiation Calculation

The incoming global solar radiation (G_{tot}) for a given location during a specific period is calculated as the sum of the direct (B_{tot}) and diffuse (D_{tot}) radiations [41,43]; the algorithm neglects the contribution of the reflected radiation because its estimation is complex, and it generally constitutes a small proportion of the total as follows:

$$G_{tot} = B_{tot} + D_{tot} \quad (1)$$

B_{tot} is the sum of the direct insolation from each sun map sector ($B_{\beta,\gamma}$) as follows:

$$B_{tot} = \Sigma\, B_{\beta,\gamma} \quad (2)$$

D_{tot} is the sum of the diffuse insolation from each sky map sector ($D_{\beta,\gamma}$) as follows:

$$D_{tot} = \Sigma\, D_{\beta,\gamma} \quad (3)$$

The direct solar radiation from the sun map sector incident on a cell defined by β and γ angles is calculated as follows:

$$B_{\beta,\gamma} = I_{SC} \cdot \tau^{m(\theta_z)} \cdot SunDur_{\beta,\gamma} \cdot SunGap_{\beta,\gamma} \cdot cos(\theta) \quad (4)$$

where I_{SC} is the solar constant, representing the solar flux outside the atmosphere. The value considered is at the mean Earth–sun distance and, according to the World Radiation Center (WRC), has a value of 1367 W/m² [44]; τ is the transmittance of the atmosphere (averaged over all the wavelengths); θ_z is the zenith angle; $SunDur_{\beta,\gamma}$ is the equivalent time duration of the sky sector; $SunGap_{\beta,\gamma}$ is the gap fraction of the sun map sector; and θ is the angle of the incidence between a line collinear with the sun's rays and the normal to the surface calculated as follows [40,41,45]:

$$\theta = arcos[cos(\beta) \cdot cos(\theta_z) + sin(\beta) \cdot sin(\theta_z) \cdot cos(\psi - \gamma)] \quad (5)$$

where $m(\theta_z)$ is the relative optical air mass, which is the ratio between the length of the optical path described by the solar photons along the oblique trajectory and the length of the optical atmospheric path in the zenith direction. For zenith angles up to 89°, it can be calculated using the following equation [43,46]:

$$m(\theta_z) = \frac{e^{-0.0001184 \cdot h}}{cos(\theta_z) + 0.50572\ (\theta_z + 6.07995)^{-1.6364}} \quad (6)$$

where h is the ground elevation above sea level.

The diffuse solar radiation from the sky map sector incident on a cell is calculated as follows:

$$D_{\beta,\gamma} = P_{dif} \cdot G_n \cdot Dur \cdot SkyGap_{\beta,\gamma} \cdot Weight_{\beta,\gamma} \cdot cos(\theta) \quad (7)$$

where P_{dif} is the diffuse proportion, indicating the fraction of the global normal radiation that is diffuse; G_n is the global normal radiation; Dur is the time interval for the analysis; $SkyGap_{\beta,\gamma}$ is the gap fraction for the sky sector; and $Weight_{\beta,\gamma}$ is the proportion of the diffuse radiation related to a sky sector with respect to all the sectors.

The global normal radiation is calculable as the sum of the direct radiation from each sector without correction for the angle of the incidence and divided by the proportion of the direct radiation ($1 - P_{dif}$) as follows:

$$G_n = \frac{I_{SC}\, \Sigma\left(\tau^{m(\theta_z)}\right)}{1 - P_{dif}} \quad (8)$$

For the uniform sky diffuse model, it is calculated as follows:

$$Weight_{\beta,\gamma} = \frac{(cos\theta_2 - cos\theta_1)}{Div_{azi}} \quad (9)$$

For the standard overcast sky model, it is calculated as follows:

$$Weight_{\beta,\gamma} = \frac{(2 \cdot cos\theta_2 + cos2\theta_2 - 2 \cdot cos\theta_1 - cos2\theta_1)}{4 \cdot Div_{azi}} \quad (10)$$

where θ_1 and θ_2 are the bounding zenith angles of the sky sector, and Div_{azi} is the number of azimuthal divisions of the sky sector.

2.2. Input Data Settings

The *Area Solar Radiation* tool requires some user-defined input parameters [33]. For the present study, these parameters are set aiming at a good tradeoff between the accuracy of the results and a reasonable calculation time. The input raster (DEM), latitude, diffuse proportion, and transmissivity will be introduced in the next sections. The rest of the input settings are introduced in Table 1 as follows:

- The sky size defines the resolution of the viewshed, the sun map, and the sky map rasters. Its value refers to the number of grid cells per side (rows and columns). A value of 200 is, therefore, chosen for the sky size, being a good compromise between time consumption and accuracy;
- The time configuration specifies the time for which the insolation is to be calculated. The chosen periods are monthly intervals, selecting the numbers of the start and end days out of 365 (366 for leap years, as in the case of 2020). Notice that the end day is exclusive in the period considered (e.g., the January start–end days are 1–32);
- The time interval is used for the calculation of the sky sectors for the sun map. To ensure high precision, a daily interval through the year and a 0.5-h interval through the day have been chosen;
- By selecting the "flat surface" option, the calculation will be performed considering the irradiation on a horizontal surface;
- The Z factor has the function to convert the surface's z units when they differ from the ground's x and y units. By converting all the data in a meter-projected coordinate system, the Z factor can be set at a value of 1;
- The number of directions refers to the viewshed calculation. For a natural terrain at a 30-meter resolution, fewer directions are sufficient (16 or 32);
- The values of the azimuth and zenith divisions, used to create sky sectors in the sky map, need to be multiples of 8;
- By selecting the "standard overcast sky" diffuse model type, the incoming diffuse radiation flux varies with the zenith angle.

Table 1. Input settings for the solar analysis.

Input	Value
Sky size/Resolution	200 cells
Time configuration	Multiple days in a year (2020, Start day, and End day)
Day interval	3 days
Hour interval	0.5 h
Z factor	1
Slope and aspect input type	Flat surface
Calculation directions	32 directions
Sky zenith divisions	16 divisions
Sky azimuth divisions	16 divisions
Diffuse model type	Standard overcast sky

2.2.1. Digital Elevation Model

A DEM is a dataset composed of points or grid cells associated with latitude–longitude location references and the respective values of the altitude. It is possible to make a distinction between two types of models: the digital terrain model (DTM) and digital surface model (DSM). Although the first one refers exclusively to the ground surface, a DSM also includes vegetation and anthropic elements. The main index of the DEM quality is its cellular resolution. Of course, minimizing the topographic generalization is a key step in order to obtain a high-quality calculation [47].

The "Advanced Land Observation System (ALOS) World 3D–30 m (AW3D30) Digital Surface Model" is the input elevation surface data selected for this case study. This is a global digital surface model dataset with a horizontal resolution of approximately 30 m (1 arcsec). It was released in 2015 by the Japan Aerospace Exploration Agency's (JAXA's) Earth Observation Research Center in a free-of-charge version available upon registration [48]. A mosaic of the area formed by five tiles, which includes the province of Matanzas (N022W081, N022W082, N022W083, N023W081, and N023W082), has been downloaded and properly cut and merged through ArcGIS tools. Because the insolation is influenced by the horizon angle, which depends on the surrounding topography, the area considered was extended beyond the borders of the province itself.

Figure 1 shows the DEM used as the input raster for the solar radiation calculation. Each pixel of the map represents an area of 30 × 30 meters approximately. To highlight the effective study area, a map of the province of Matanzas was overlaid.

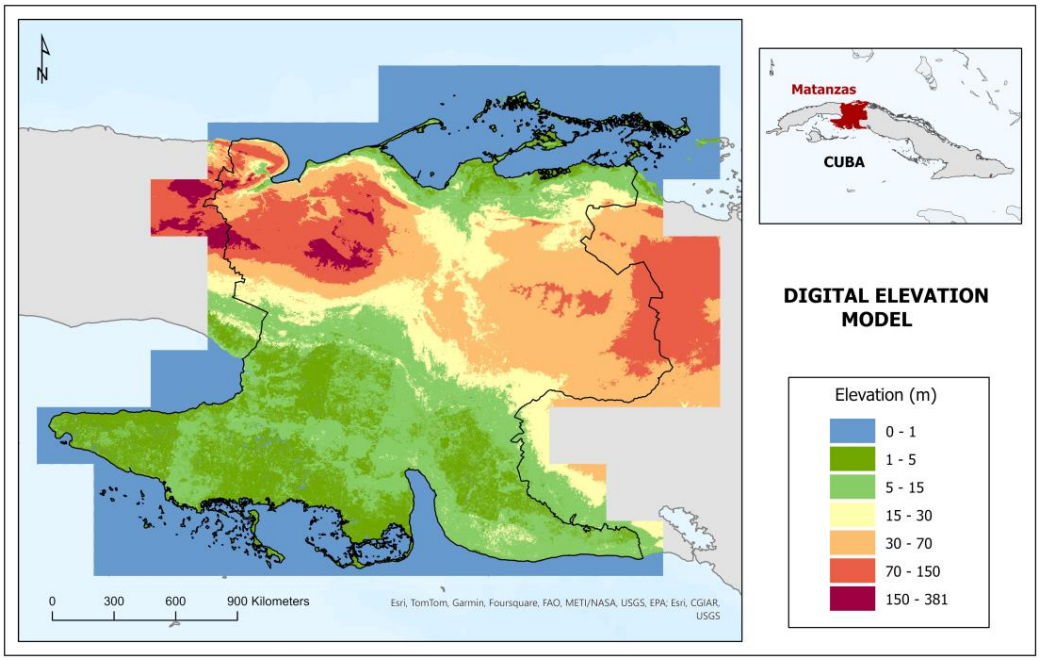

Figure 1. DEM of the province of Matanzas.

2.2.2. Latitude

The site's latitude is automatically set based on the geographical coordinates of the centroid of the DEM uploaded. This solar radiation tool was mainly designed for local scales, and if the study area is small, considering the same latitude for each cell is an acceptable approximation in the calculations of the solar position and declination. When large areas, such as regions, countries, or continents, are analyzed, the latitude can vary considerably between the different areas, affecting the results of the solar radiation. This tool does not allow us to set multiple values of the latitude; therefore, the large geographical areas have to be divided into smaller study areas with different latitudes (no greater than 1 decimal degree) [33]. The same consideration is valid for the clearness index and diffuse ratio, a single value per zone, so both parameters will be determined for each of the divisions. The province of Matanzas, which is a substantially larger area, was divided into smaller subareas for this purpose. The DEM presented in Figure 2 has been divided into 80 square rows with a size of 0.15 × 0.15 decimal degrees. Each block has been numbered proceeding from west to east and from south to north. This is one of the fundamental and most innovative aspects of the method proposed in this research.

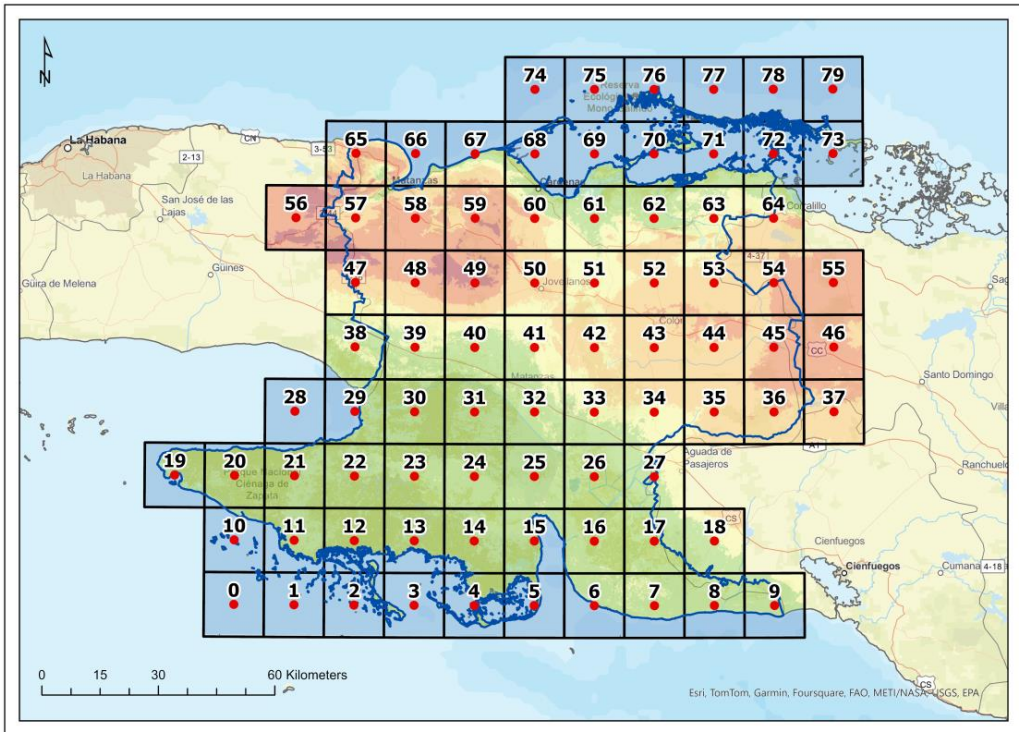

Figure 2. Matanzas province's DEM, including division for further analysis.

At this latitude, an extension of 0.15 degrees corresponds to approximately 16 km, which makes the surface of each cell about 256 km^2. Compartmentalizing the territory this way responds to the need to combine in ArcGIS a homogeneous distribution of the parameters extracted from Meteonorm with their characteristics and processing times. The result adequately reflects the solar resource distribution at the provincial scale. Although the level of the detail shown in Guasasa might not be enough, it is adequate in this case because of the very low variability of the resource for being a practically flat terrain in a very limited area.

2.2.3. Diffuse Proportion and Clearness Index

Crossing the atmosphere and colliding against its molecules and particles, a portion of the solar flux is affected by the phenomena of absorption and scattering. This interaction is responsible for the attenuation of the solar radiation hitting Earth's surface and involves

gases (CO_2, O_2, O_3, and other air molecules), solid particulate matter, liquid particles (aerosols, including non-condensed water), and clouds (condensed water) [49]. The influence of these factors is higher when the probability of the interaction with the solar flux increases, so it depends on the distance crossed by the sunbeams, the variability of the air's composition (e.g., because of pollution), and weather conditions.

The *Area Solar Radiation* tool does not consider the variability of the atmospheric conditions in time and space, a limitation highlighted by the developers themselves [39]. In order to deal with this aspect, the current analysis set different values of the input clearness index and diffuse proportion for each of the 80 divisions, in relation to the period considered, thus bringing novelty to the proposed methodology.

The *diffuse proportion, or cloudiness index* (K_D), is defined as the ratio of the diffuse solar radiation to the global solar radiation measured at Earth's surface. The value range of the diffuse proportion is considered in ArcGIS from 0 to 1, depending on the atmospheric conditions. Usually, a value of 0.2 is considered for very clear sky conditions and 0.3 for clear sky conditions. It can be calculated [40,50] as follows:

$$K_D = \frac{D_{tot}}{G_{tot}} \tag{11}$$

In the case of the *clearness index, or atmospheric transmissivity* (K_T), it is considered as the ratio of the global solar radiation measured at Earth's surface to the extraterrestrial solar radiation at the top of the atmosphere. Values range from 0 (no transmission) to 1 (complete transmission). Typically observed values are 0.6 or 0.7 for very clear sky conditions and 0.5 for only a generally clear sky. The clearness index has an inverse relation with the diffuse proportion parameter [33], and it is calculated [40,50] as follows:

$$K_T = \frac{G_{tot}}{I_{SC} \cdot \varepsilon \cdot cos(\theta_z)} \tag{12}$$

where ε represents Earth's orbital eccentricity relative to the nth day of the year and is calculated as follows [40,45]:

$$\varepsilon = 1 + 0.0334 \cdot \cos\left(n \cdot \frac{2\pi}{365.25}\right) \tag{13}$$

The scientific literature proposes many models for the estimation of K_T and K_D, influenced by the stochastic nature of the cloud attenuation process. Statistical time series models can be reliable to forecast the clearness index in the long term, while more recent forecasting models, based on machine-learning approaches, are more effective for short-term predictions [51]. The atmospheric transmissivity, according to the Lambert–Beer law of the radiation extinction, has an inverse exponential relationship with the atmospheric optical depth, which is the sum of the optical depth of each atmospheric component [52]. However, because of the complexity and a lack of data, which, in this analysis, should be spatially distributed, an empirical approach was preferred. Starting from historical data of solar radiation, it is possible to derive the monthly average clearness index and diffuse ratio related to each considered area.

The calculation of the monthly mean values of K_T and K_D requires monthly mean global horizontal and diffuse radiation data for the 80 selected areas represented by the centroid coordinates (Figure 2). To obtain these values, Meteonorm software, Version 7, has been used [20,53]. Meteonorm is a comprehensive meteorological database containing climatological data for solar engineering applications anywhere in the world. This software combines a large dataset from all over the world with numerous computational models, being able to generate statistically representative meteorological sequences for the desired location's typical meteorological year (TMY).

The radiation database refers to 20-year measurement periods, while the other meteorological parameters are based on monthly averages calculated during the 1961–1990 and 2000–2009 periods. Such weather station data are adapted to each location through space-dependent interpolation, considering the altitude, topography, region, etc. In particular, for

global radiation, the interpolation procedure uses a 3D inverse distance model (Shepard's gravity interpolation). Diffuse radiation is derived from global radiation through the dynamic model of Perez [54], which takes into account its anisotropic behavior concentrated in the circumsolar zone and near the horizon [40].

Once the list of 80 locations is imported using the batch mode function of Meteonorm, the calculation settings have to be defined as follows:

- The "future" field has been selected as the climatological time period, allowing us to choose between three different future scenarios from the IPCC report of 2007 as follows [55]: B1 (low), A1B (mid), and A2 (high). The option A1B (in the year 2020) has been chosen and is characterized by a forecast of a more integrated world, with a balanced emphasis on all the energy sources;
- The "interpolated" field has been set for the atmospheric turbidity based on satellite data from the satellite experiments MISR and MODIS [53];
- A personalized output format has been selected, setting the monthly global, diffuse, and extraterrestrial radiations as the output format of the calculation.

In the first step of the calculation, the software searches for the closest weather stations to each selected location, and their long-term monthly means are interpolated. The whole set of weather stations used by the current calculation is as follows: La Fe, Havana/Jose Marti, Casa Blanca, Camaguey, and Key West, FL. In the second step, a stochastic weather generator to create a TMY of the data with the selected time resolution (hourly) runs the interpolated monthly data. The results have finally been exported and used to calculate the monthly mean K_T and K_D values for each location, using Equations (11) and (12).

3. Results

The first key outcome of this study is the successful application of the methodology outlined in the previous section. This approach demonstrates how enhanced accuracy can be achieved through the effective combination of a tessellation procedure with a specific parameterization. This parameterization is derived from an external database, in this case, solar radiation data sourced from ArcGIS.

Second, we present two comparative maps illustrating the cartographic outcomes of our methodology. The first map displays solar radiation data for the entire province, showcasing a large geographical area typically not analyzed at such a high resolution. This territory possesses significant potential for solar energy utilization because of its specific characteristics. The second map focuses on the detailed analysis of a smaller locality, Guasasa. This area was selected because it lies outside the established electricity grid and represents a promising candidate for autonomous electrification using renewable energy sources.

3.1. Validation and Corrections of Diffuse Proportion and Clearness Index

The values of K_T and K_D need to be validated before being used as clearness index and diffuse proportion input for the execution of the *Area Solar Radiation*. An effective method to validate these parameters is to run the solar radiation calculation and compare the outputs with the results provided by Meteonorm, which represents a reliable source, according to the previous section.

For this task, *Point Solar Radiation* is an ArcGIS tool [56] belonging to the same *Spatial Analyst* extension as Area Solar Radiation. The required input parameters and the equations used are the same for both, except the location where the calculation is run: Point Solar Radiation derives incoming solar radiation for specific locations that can be loaded in the format of a point feature class or a table of point coordinates. This implies a short calculation time and allows us to compare directly the results with the expected values.

Like in Meteonorm calculations, the centroid coordinates of each of the 80 zones are set as input locations for a Point Solar Radiation calculation. At this point, the main issue is the necessity for running a calculation with multiple input settings with a tool that only allows us to set unique values of the clearness index and diffuse proportion.

This problem can be solved by implementing a Python script that cyclically executes for the 80 grids' central points, the Point Solar Radiation function from the "arcpy" environment. This script is run for each month of the year and sequentially loads the DEM raster file of the zone in which the point is located, its latitude, and the monthly K_T and K_D values. Once the monthly global, direct, and diffuse radiations are calculated for each of the 80 points, the outputs are merged into three single files.

The output radiation generated by the script execution differs significantly from the value estimated using Meteonorm. The monthly mean errors, calculated as percentages of the Meteonorm values and averaged for all 80 study areas, are presented in Table 2, separated as global (err% glob.), direct (err% dir.), and diffuse (err% diff.) radiations.

Table 2. Mean error percentages of the Point Solar Radiation calculations in relation to the monthly Meteonorm values.

	Jan.	**Feb.**	**Mar.**	**Apr.**	**May**	**Jun.**	**Jul.**	**Aug.**	**Sep.**	**Oct.**	**Nov.**	**Dec.**
err% glob.	−8.7	12.0	18.6	23.9	30.1	23.5	30.4	37.2	35.4	21.9	−0.4	−20.0
err% dir.	−12.2	17.6	28.9	39.9	46.5	30.5	46.2	57.4	54.3	32.1	−1.4	−36.9
err% diff.	−2.7	4.7	4.0	0.8	10.2	16.7	11.5	16.3	18.9	12.5	1.7	1.1

As can be noticed in Equation (4), the calculation of the direct radiation depends on a fixed solar constant, without taking into account how Earth's orbital eccentricity influences the incoming irradiance. Considering the effect of the sun's distance variability over the year, Equation (13) represents the first correction factor to reduce the error. The following equation [40,45] can be used to calculate the extraterrestrial normal radiation ($I_{0,n}$):

$$I_{0,n} = I_{sc} \cdot \varepsilon \tag{14}$$

by taking into account that for each month, we must use the middle day of the month as the n input value in Equation (14). Accounting for the eccentricity effect on the direct radiation directly mitigates the error, as can be seen in Table 3.

Table 3. Mean error percentages of the 80 Point Solar Radiation calculations, accounting for the eccentricity effect, compared to the monthly Meteonorm values.

	Jan.	**Feb.**	**Mar.**	**Apr.**	**May**	**Jun.**	**Jul.**	**Aug.**	**Sep.**	**Oct.**	**Nov.**	**Dec.**
err% glob.	−5.8	14.5	19.7	22.9	27.2	19.6	26.3	34.0	34.3	22.9	1.9	−17.5
err% dir.	−9.6	20.3	30.1	38.8	43.2	26.4	41.6	53.8	53.0	33.2	0.9	−34.9
err% diff.	−0.5	7.0	5.0	0.0	7.7	13.0	7.9	13.5	17.9	13.5	4.0	4.3

The correction of the input values of the clearness index and diffuse proportion is still needed to minimize the discrepancy and achieve better accuracy. The clearness index input required by the ArcGIS tool refers to the condition of the zero altitude, while the calculated K_T refers to the actual conditions at the respective sites. The average error was, therefore, predictable. However, the existing heterogeneity across the different areas reflects a good approximation of the variability because of weather conditions forecast. By applying the same correction factor to each area, such variability accuracy is preserved.

The first step is focused on minimizing the percentage error of the direct radiation. The K_T values have been modified with a percentage variation of ±5%, and different executions of the script have been performed, investigating the modified K_T that produces the most accurate direct radiation output (in comparison to the Meteonorm values) for each month. Table 4 shows the errors of the outputs produced using $K_{T,mod}$ and K_D as the inputs of the calculations, where $K_{T,mod}$ is the clearness index value that minimizes the direct radiation error. The second row shows the applied variation from the original K_T values.

Table 4. Average percentages of calculation errors for the solar radiation in Matanzas province, obtained from 80 points, compared to the monthly values of the Meteonorm, using the modified clearness index ($K_{T,mod}$) as the input of the transmissivity.

	Jan.	Feb.	Mar.	Apr.	May	Jun.	Jul.	Aug.	Sep.	Oct.	Nov.	Dec.
K_T mod.	+5%	−10%	−20%	−20%	−25%	−15%	−25%	−30%	−25%	−15%	–	+25%
err% glob.	2.6	−2.7	−9.5	−8.1	−12.0	−3.0	−7.8	−15.4	−9.2	−4.2	1.9	25.6
err% dir.	−1.7	2.8	−0.5	3.0	0.1	3.2	−1.2	−1.6	4.3	4.4	0.9	−1.4
err% diff.	9.5	−9.8	−22.3	−27.0	−27.2	−9.5	−27.0	−30.0	−21.9	−12.6	4.0	58.4

The diffuse radiation is calculated depending on the global normal radiation (G_n) (Equation (8)), which also depends on the direct radiation, as can be seen in Equation (8). For this reason, the direct radiation needs to be corrected first. The second step is to minimize the gap of the diffuse radiation. Following the same procedure, modified values of K_D, with a percentage variation of ±5%, have been tested and coupled with $K_{T,mod}$ as inputs of the point solar radiation script. The chosen couples of $K_{T,mod}$ and $K_{D,mod}$ are the ones that produced the minimum errors, as reported in Table 5.

Table 5. Average percentages of the calculation errors for the solar radiation in Matanzas province, obtained from 80 points, compared to the monthly values of the Meteonorm, using the modified clearness index ($K_{T,mod}$) as the input of the transmissivity and the modified diffuse ratio ($K_{D,mod}$) as the input of the diffuse proportion.

	Jan.	Feb.	Mar.	Apr.	May	Jun.	Jul.	Aug.	Sep.	Oct.	Nov.	Dec.
K_T mod.	+5%	−10%	−20%	−20%	−25%	−15%	−25%	−30%	−25%	−15%	–	+25%
K_D mod.	−5%	+5%	+15%	+15%	+20%	+5%	+20%	+20%	+10%	+5%	–	−25%
err% glob.	−0.8	1.0	−0.2	0.7	2.0	1.5	1.6	0.9	0.3	0.6	1.9	−1.4
err% dir.	−1.7	2.8	−0.5	3.0	0.1	3.2	−1.2	−1.6	4.3	4.4	0.9	−1.4
err% diff.	0.8	−1.4	0.0	−6.4	4.2	−0.3	4.8	3.6	−3.6	−3.2	4.0	−1.5

The second row shows the applied variations with respect to the original K_T and K_D values.

A comparison is useful to visualize the trend and the correction. The monthly global, direct, and diffuse horizontal irradiations have been calculated for the 80 point-locations identified along the province of Matanzas. The average values among the 80 locations have been used to compare the outputs calculated using Point Solar Radiation with the reference values calculated using Meteonorm. By properly adjusting the input values of K_T and K_D, the error between the two calculations has been minimized.

In the Tables 6–8 and Figures 3–5, "point solar" refers to the outputs calculated before the correction, while "corrected" refers to the outputs calculated using the modified $K_{T,mod}$ and $K_{D,mod}$.

Table 6. Monthly global horizontal irradiations calculated through Meteonorm (first row), point solar with original values of K_T and K_D (second row), and point solar with corrected values of $K_{T,mod}$ and $K_{D,mod}$ (third row).

Global Horizontal Irradiation (kWh/m²)												
	Jan.	Feb.	Mar.	Apr.	May	Jun.	Jul.	Aug.	Sep.	Oct.	Nov.	Dec.
Meteonorm	121.6	129.3	167.8	182.7	187.4	170.6	186.1	172.7	145.0	130.8	118.9	107.7
Point Solar	111.0	144.8	199.0	226.4	243.9	210.7	242.7	237.0	196.4	159.4	118.4	86.1
Corrected	120.6	130.5	167.4	184.0	191.3	173.1	189.1	174.4	145.5	131.6	121.2	106.1

Table 7. Monthly direct horizontal irradiations calculated through Meteonorm (first row), point solar with original values of K_T and K_D (second row), and point solar with corrected values of $K_{T,mod}$ and $K_{D,mod}$ (third row).

Direct Horizontal Irradiation (kWh/m²)												
	Jan.	**Feb.**	**Mar.**	**Apr.**	**May**	**Jun.**	**Jul.**	**Aug.**	**Sep.**	**Oct.**	**Nov.**	**Dec.**
Meteonorm	74.6	73.1	98.5	108.8	104.6	88.0	103.1	89.6	71.0	64.7	57.5	59.5
Point Solar	65.5	86.0	127.0	152.2	153.2	114.9	150.7	141.0	109.5	85.5	66.6	37.5
Corrected	73.4	75.2	98.1	112.1	104.7	90.8	101.9	88.2	74.0	67.6	68.1	58.6

Table 8. Monthly diffuse irradiations calculated through Meteonorm (first row), point solar with original values of K_T and K_D (second row), and point solar with corrected values of $K_{T,mod}$ and $K_{D,mod}$ (third row).

Diffuse Irradiation (kWh/m²)												
	Jan.	**Feb.**	**Mar.**	**Apr.**	**May**	**Jun.**	**Jul.**	**Aug.**	**Sep.**	**Oct.**	**Nov.**	**Dec.**
Meteonorm	47.0	56.2	69.4	74.1	83.0	82.5	83.2	83.1	74.1	66.2	51.3	48.3
Point Solar	45.7	58.8	72.2	74.7	91.4	96.3	92.7	96.7	88.0	74.4	52.1	48.8
Corrected	47.4	55.4	69.3	69.4	86.5	82.3	87.1	86.1	71.4	54.0	53.3	47.5

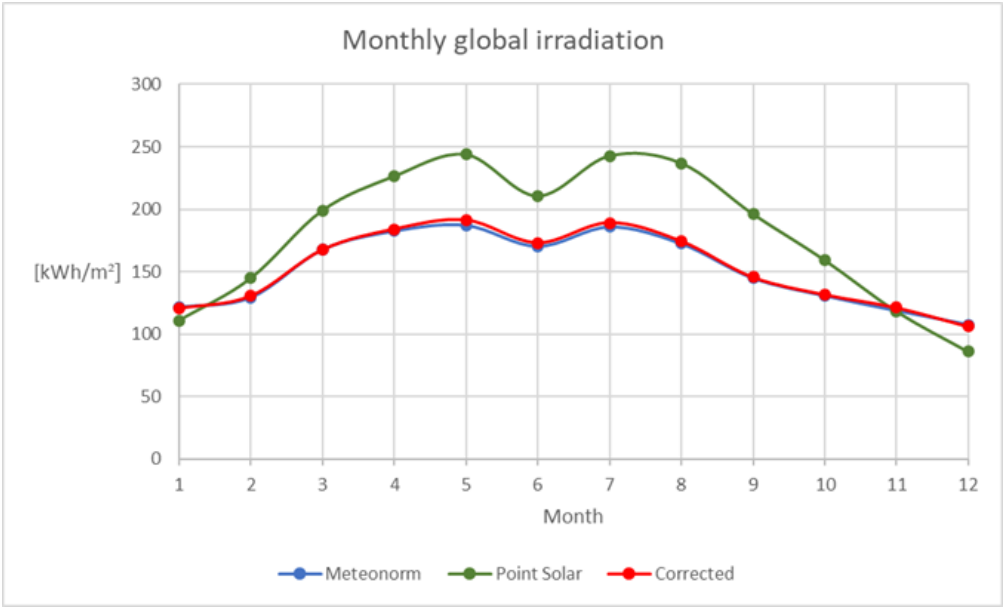

Figure 3. The trends of the monthly global horizontal irradiations calculated through Meteonorm (blue), point solar with original values of K_T and K_D (green), and point solar with corrected values of K_T and K_D (red).

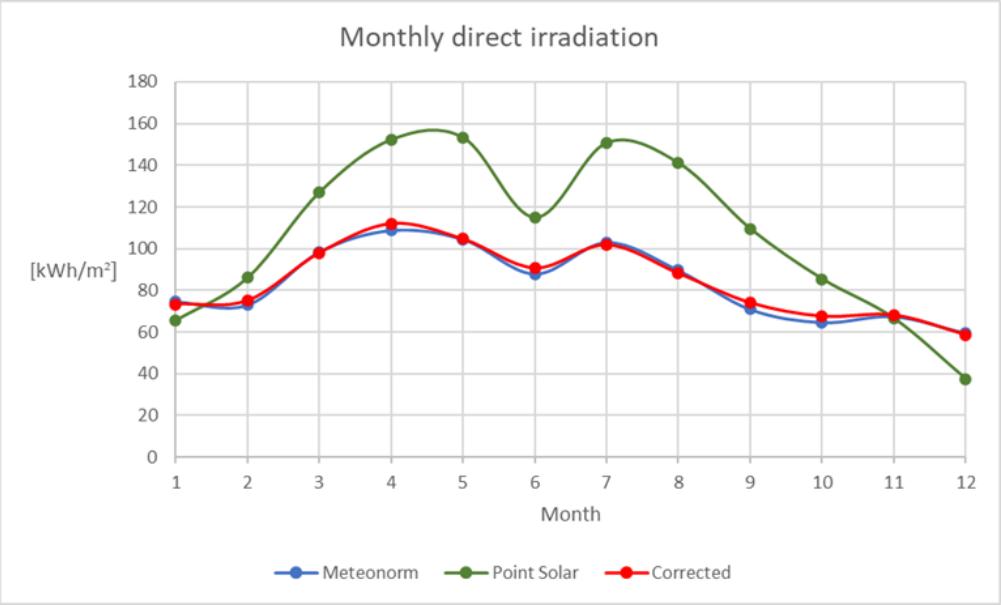

Figure 4. The trends of the monthly direct horizontal irradiations calculated through Meteonorm (blue), point solar with original values of K_T and K_D (green), and point solar with corrected values of K_T and K_D (red).

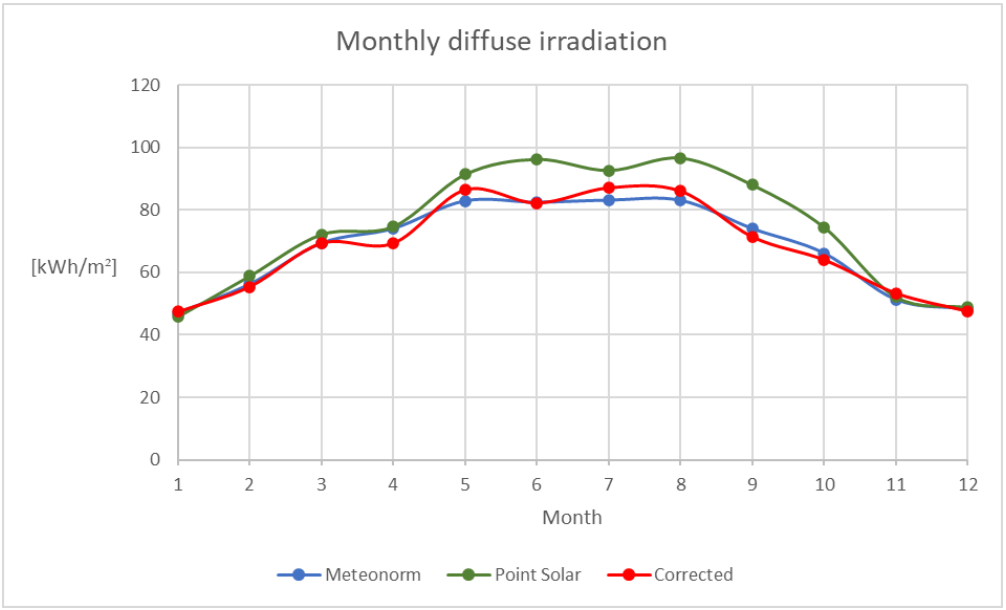

Figure 5. The trends of the monthly diffuse irradiations calculated through Meteonorm (blue), point solar with original values of K_T and K_D (green), and point solar with corrected values of K_T and K_D (red).

3.2. Matanzas Province's Solar Radiation Map

Once the input parameters required by the *Area Solar Radiation* tool are provided, it is possible to proceed to the creation of the solar maps. In the same way as for the *Point Solar Radiation* tool, a script is required to run the calculations with different inputs for each zone. The two scripts have a similar structure: a number of fixed input settings are combined with variable input settings that are iteratively taken from the parameters of a single zone, including the latitude, clearness index, and diffuse proportion. In addition to them, the script sets the extent of the portion of the total raster's DEM that will be processed by the tool. For each loop generated by the script, the extent of the area needs to be defined by setting the coordinates of their opposite corners. Each time the command is executed, it

generates a portion of the global solar map. When the loop comes to the last iteration, all the portions are merged into a single raster using the tool *Mosaic to new raster*. The following settings are chosen for the mosaic: the pixel type is 32_BIT_FLOATING; the number of bands is 1; the mosaic method is MEAN; the mosaic color map mode is FIRST. This means that the output cellular values of the overlapping areas are the average values of the overlapping cell, and the color map of the first raster dataset will be applied to all the raster mosaic. The extent environment borders exceed the size area of each zone in order to flatten the gap between contiguous areas. The 80 zones identified have a size of 0.15×0.15 decimal degrees, while the chosen size of the extnt area is 0.225×0.225 decimal degrees.

Finally, the resulting monthly solar maps of Matanzas are summed and merged. The map obtained (Figure 6) represents the annual global horizontal irradiation in Matanzas. The high resolution is hidden by the large scale of the area considered. A closer view would highlight the variation of the solar radiation pixel by pixel. In the northern part of the province, characterized by a mountainous landscape, a higher level of radiation is visible along the slopes. The relevance of this result is that any portion of this wide area can be extracted and used for eventual future studies.

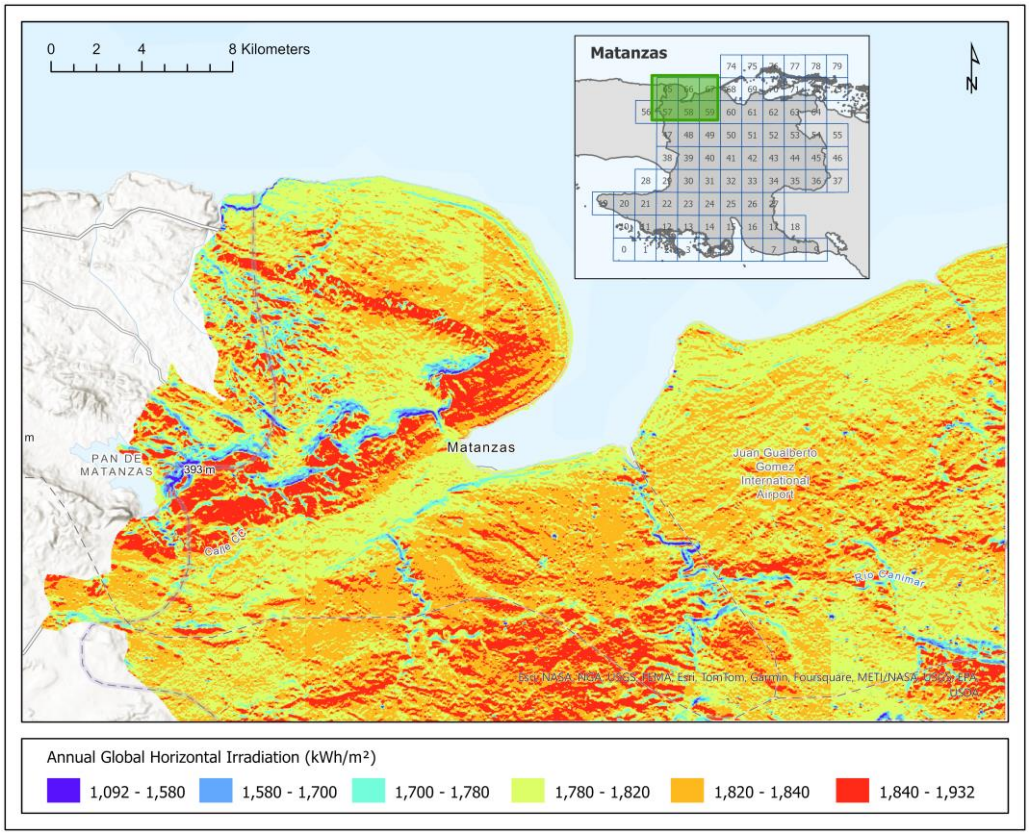

Figure 6. Annual global horizontal irradiation in Matanzas.

3.3. Guasasa's Solar Radiation Map

To conclude, from the solar radiation map of the province of Matanzas, we have to obtain the radiation values of the study area in the community of Guasasa (Figure 7). The calculated map of Matanzas refers to the global horizontal irradiation (G_H), and it is necessary to determine the radiation available for a PV installation on the buildings distributed in the community. The assessment of the PV potential requires as input the solar radiation received by the solar panels' surfaces, that is, by tilted surfaces. The surface angle considered is the optimal tilt angle (β_{opt}). In order to calculate the global irradiation on the optimal tilted surface, a correction factor is needed.

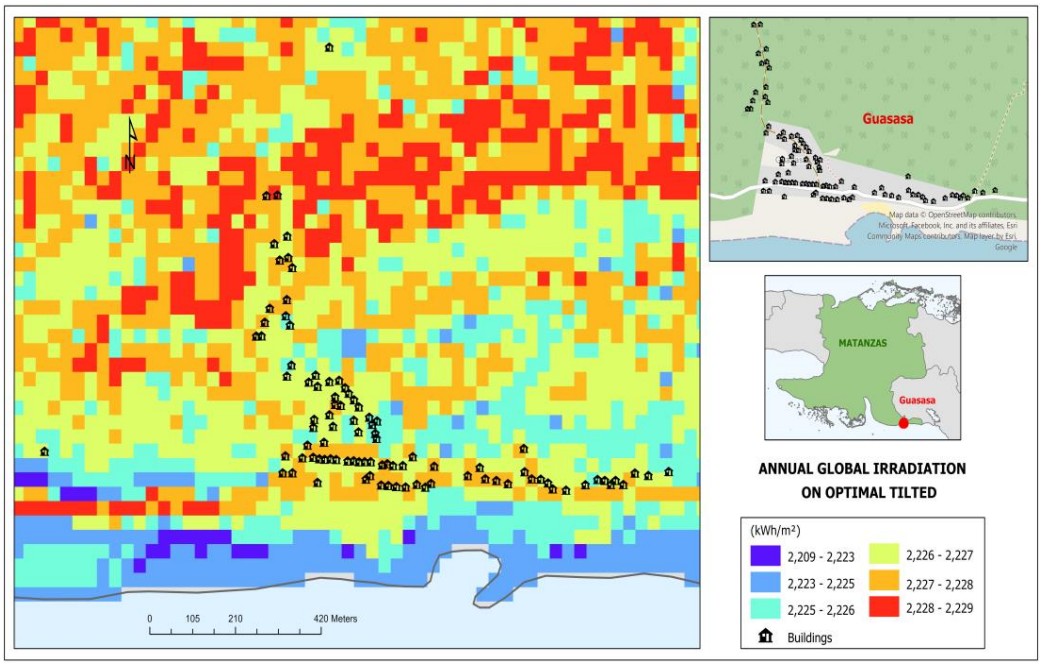

Figure 7. Annual global irradiation on optimal tilted surface in Guasasa (Matanzas).

By setting the coordinates of Guasasa on the PVGIS web map [28], the monthly average values of G_H and $G_{\beta opt}$ are downloaded. The period considered for the data collection is from 2001 to 2020. The ratio of each couple of values is calculated as follows, and the average value of each ratio is considered as a correction factor (K_β):

$$K_\beta = \frac{G_{\beta_{opt}}}{G_H} = 1.088 \quad (15)$$

As shown in Figure 7, by multiplying the factor K_β for each pixel of the annual G_H raster, a new raster representing $G_{\beta opt}$ is obtained.

4. Discussion and Conclusions

A series of twelve maps, one for each month of the year, is created and merged in order to provide a value for each pixel of the average annual radiation received. The shadows originated by both the morphology and the horizon characteristics are considered in the calculation. This study includes the implementation of a Python script for the cyclic execution of the *Area Solar Radiation* with the aim for bypassing the limitation of the tool in performing the calculation for large areas. Indeed, the input settings only allow for the insertion of single values for the definition of the atmospheric influence on the solar radiation, a condition that may vary considerably over time and space. The validation is conducted through the software Meteonorm, version 7.

Meteonorm is a widely used solar radiation data source in the solar energy industry. Its reliable database provides punctual values of solar radiation for any desired site. By selecting an adequate number of locations, it is possible to compare the results with the output derived from the ArcGIS calculation. In order to facilitate the comparison, a second Python script is implemented for the cyclical execution of the *Point Solar Radiation*, another ArcGIS tool. It has the same architecture as that of the *Area Solar Radiation* but is designed for the calculation of specific point locations. This comparison allows us to investigate and perform the necessary corrections of the input tool's settings so that the outputs of the *Area Solar Radiation* have the minimal error with respect to the experimental measurements.

This development presents a high-resolution solar radiation map for Matanzas, Cuba, utilizing a novel methodology to enhance the accuracy of solar radiation calculations over extensive areas. This study highlights the potential of commercial software for solar

radiation analysis across various scales, demonstrating how precise application requires adapting parameters to the specific conditions of the study area and validating results against other available databases or programs. The development and implementation of customized scripts, as illustrated by our methodology, can significantly improve the accuracy and relevance of solar radiation mapping. Thus, the approach presented herein not only advances solar radiation mapping for Matanzas but also serves as a valuable reference for similar studies aiming to refine solar energy assessments in diverse contexts.

Author Contributions: Direction of the research, J.D. and L.F.Z.; conceptualization, J.D. and L.F.Z.; methodology, J.D., C.B., A.M.M. and L.F.Z.; software and validation, C.B. and A.M.M.; writing—original draft preparation, C.B. and J.D.; writing—review and editing, all the authors; scientific supervision, J.D. and L.F.Z.; project administration, J.D.; funding acquisition, J.D. All authors have read and agreed to the published version of the manuscript.

Funding: This research was funded by the Spanish Agency for International Development Cooperation (AECID), grant number 2018/ACDE/000600, under the innovation action HIBRI2, and by the ERASMUS + program of the European Union (I-PADOVA01).

Institutional Review Board Statement: Not applicable.

Informed Consent Statement: Not applicable.

Data Availability Statement: The original contributions presented in this study are included in the article; further inquiries can be directed to the corresponding author.

Acknowledgments: We would like to express our recognition of the fundamental work conducted at the HIBRI2 project of the Cuban Center for Information Management and Energy Development (CUBAENERGÍA) as well as the NGO Cuban Society for the Promotion of Renewable Energy Sources and Respect for the Environment (CUBASOLAR). Special thanks to the people of Guasasa and the municipality's authorities.

Conflicts of Interest: The authors declare no conflicts of interest.

References

1. IEA. SDG7: Data and Projections. Available online: https://www.iea.org/reports/sdg7-data-and-projections (accessed on 10 August 2024).
2. Domínguez Bravo, J. *Los Sistemas de Información Geográfica en la Planificación e Integración de Energías Renovables*; CIEMAT: Madrid, Spain, 2002; p. 159.
3. Domínguez, J.; Arribas, L.; de Diego, L.; Herrera, I.; Zarzalejo, L. *Sistema Integrado de Control Para el Abastecimiento de Energía Mediante Sistemas Híbridos en Comunidades Aisladas de Cuba. Fase II (Proyecto HIBRI2) 1520*; CIEMAT: Madrid, Spain, 2022; p. 62. Available online: https://www.ciemat.es/portal.do?TR=A&IDR=1&identificador=1046 (accessed on 9 September 2024).
4. Domínguez, J.; Bellini, C.; Arribas, L.; Amador, J.; Torres-Pérez, M.; Martín, A.M. IntiGIS-Local: A Geospatial Approach to Assessing Rural Electrification Alternatives for Sustainable Socio-Economic Development in Isolated Communities—A Case Study of Guasasa, Cuba. *Energies* **2024**, *17*, 3835. [CrossRef]
5. Benalcazar, P.; Komorowska, A.; Kamiński, J. A GIS-based method for assessing the economics of utility-scale photovoltaic systems. *Appl. Energy* **2024**, *353*, 122044. [CrossRef]
6. Gacu, J.G.; Garcia, J.D.; Fetalvero, E.G.; Catajay-Mani, M.P.; Monjardin, C.E.F. Suitability Analysis Using GIS-Based Analytic Hierarchy Process (AHP) for Solar Power Exploration. *Energies* **2023**, *16*, 6724. [CrossRef]
7. Ibraheem, I.F. Remote sensing data and environmental parameters usage for the establishment of a mapping of solar energy potential in Iraq. *AIP Conf. Proc.* **2023**, *2787*, 080032. [CrossRef]
8. Kanters, J.; Wall, M.; Kjellsson, E. The Solar Map as a Knowledge Base for Solar Energy Use. *Energy Procedia* **2014**, *48*, 1597–1606. [CrossRef]
9. Loquias, R.; Palima, N.; Juanillas, M.; Magno, L.; Compuesto, K.; Zagada, A.; Isaac, V.; Tabal, K.M.; Terano, H.J. Suitability Mapping of Solar Energy Potential of Selected Areas in Camarines Sur using ArcGIS. *J. Eng. Emerg. Technol.* **2022**, *1*, 37–49. [CrossRef]
10. Szabó, Z.; Wang, G.; Ágnes, S. Estimating Solar Energy Potential of Hungary Based on Raster Maps. *J. Digit. Landsc. Archit.* **2023**, *8*, 112–123. [CrossRef]
11. Alrwashdeh, S.S.; Alsaraireh, F.M.; Saraireh, M.A. Solar radiation map of Jordan governorates. *Int. J. Eng. Technol.* **2018**, *7*, 1664. [CrossRef]

12. Settou, B.; Settou, N.; Gouareh, A.; Negrou, B.; Mokhtara, C.; Messaoudi, D. A high-resolution geographic information system-analytical hierarchy process-based method for solar PV power plant site selection: A case study Algeria. *Clean Technol. Environ. Policy* **2020**, *23*, 219–234. [CrossRef]
13. Hasan, A.S.M.M.; Kesapabutr, P.; Möller, B. Bangladesh's pathways to net-zero transition: Reassessing country's solar PV potential with high-resolution GIS data. *Energy Sustain. Dev.* **2024**, *81*, 101511. [CrossRef]
14. Yaiche, M.R.; Bouhanik, A.; Bekkouche, S.M.A.; Malek, A.; Benouaz, T. Revised solar maps of Algeria based on sunshine duration. *Energy Convers. Manag.* **2014**, *82*, 114–123. [CrossRef]
15. Enjavi-Arsanjani, M.; Hirbodi, K.; Yaghoubi, M. Solar Energy Potential and Performance Assessment of CSP Plants in Different Areas of Iran. *Energy Procedia* **2015**, *69*, 2039–2048. [CrossRef]
16. Jung, J.; Han, S.; Kim, B. Digital numerical map-oriented estimation of solar energy potential for site selection of photovoltaic solar panels on national highway slopes. *Appl. Energy* **2019**, *242*, 57–68. [CrossRef]
17. Kanters, J.; Wall, M. A planning process map for solar buildings in urban environments. *Renew. Sustain. Energy Rev.* **2016**, *57*, 173–185. [CrossRef]
18. Wegertseder, P.; Lund, P.; Mikkola, J.; García Alvarado, R. Combining solar resource mapping and energy system integration methods for realistic valuation of urban solar energy potential. *Sol. Energy* **2016**, *135*, 325–336. [CrossRef]
19. ESRI. ArcGIS for Desktop 10.8. Available online: https://www.esri.com/en-us/arcgis/products/arcgis-desktop/overview (accessed on 10 August 2024).
20. Meteotest. Meteonorm Software. Worldwide Irradiation Data. Available online: https://meteonorm.com/en/ (accessed on 10 August 2024).
21. EcuRed. Guasasa. Available online: https://www.ecured.cu/Guasasa (accessed on 10 August 2024).
22. Prăvălie, R.; Patriche, C.; Bandoc, G. Spatial assessment of solar energy potential at global scale. A geographical approach. *J. Clean. Prod.* **2019**, *209*, 692–721. [CrossRef]
23. Ali, S.; Taweekun, J.; Techato, K.; Waewsak, J.; Gyawali, S. GIS based site suitability assessment for wind and solar farms in Songkhla, Thailand. *Renew. Energy* **2019**, *132*, 1360–1372. [CrossRef]
24. Mahtta, R.; Joshi, P.K.; Jindal, A.K. Solar power potential mapping in India using remote sensing inputs and environmental parameters. *Renew. Energy* **2014**, *71*, 255–262. [CrossRef]
25. Pavlovic, T.M.; Milosavljevic, D.D.; Mirjanic, D.; Pantic, L.S.; Radonjic, I.S.; Pirsl, D. Assessments and perspectives of PV solar power engineering in the Republic of Srpska (Bosnia and Herzegovina). *Renew. Sustain. Energy Rev.* **2013**, *18*, 119–133. [CrossRef]
26. Solargis. Global Solar Atlas. Available online: https://globalsolaratlas.info (accessed on 10 August 2024).
27. NASA. Prediction of Wordwide Energy Resources. Available online: https://power.larc.nasa.gov/ (accessed on 10 August 2024).
28. European Commission. Photovoltaic Geographical Information System (PVGIS). Available online: https://joint-research-centre.ec.europa.eu/photovoltaic-geographical-information-system-pvgis_en (accessed on 10 August 2024).
29. Lukač, N.; Žlaus, D.; Seme, S.; Žalik, B.; Štumberger, G. Rating of roofs' surfaces regarding their solar potential and suitability for PV systems, based on LiDAR data. *Appl. Energy* **2013**, *102*, 803–812. [CrossRef]
30. Antonanzas, J.; Urraca, R.; Martinez-de-Pison, F.J.; Antonanzas-Torres, F. Solar irradiation mapping with exogenous data from support vector regression machines estimations. *Energy Convers. Manag.* **2015**, *100*, 380–390. [CrossRef]
31. Srećković, N.; Lukač, N.; Žalik, B.; Štumberger, G. Determining roof surfaces suitable for the installation of PV (photovoltaic) systems, based on LiDAR (Light Detection and Ranging) data, pyranometer measurements, and distribution network configuration. *Energy* **2016**, *96*, 404–414. [CrossRef]
32. Martín, A.M.; Dominguez, J. Solar Radiation Interpolation. In *Solar Resources Mapping: Fundamentals and Applications*; Polo, J., Martín-Pomares, L., Sanfilippo, A., Eds.; Springer International Publishing: Cham, Switzerland, 2019; pp. 221–242. [CrossRef]
33. ESRI. ArcGIS Desktop. ArcMap. Area Solar Radiation. Available online: https://desktop.arcgis.com/en/arcmap/latest/tools/spatial-analyst-toolbox/area-solar-radiation.htm (accessed on 10 August 2024).
34. Santos, T.; Gomes, N.; Freire, S.; Brito, M.C.; Santos, L.; Tenedório, J.A. Applications of solar mapping in the urban environment. *Appl. Geogr.* **2014**, *51*, 48–57. [CrossRef]
35. Kausika, B.B.; van Sark, W.G.J.H.M. Calibration and Validation of ArcGIS Solar Radiation Tool for Photovoltaic Potential Determination in the Netherlands. *Energies* **2021**, *14*, 1865. [CrossRef]
36. Hofierka, J.; Šúri, M.; Huld, T. r.sun.—Solar Irradiance and Irradiation Model. Available online: https://grass.osgeo.org/grass80/manuals/r.sun.html (accessed on 10 August 2024).
37. Li, Z.Q.; Zhang, Z.D.; Davey, K. Estimating Geographical PV Potential Using LiDAR Data for Buildings in Downtown San Francisco. *Trans. GIS* **2015**, *19*, 930–963. [CrossRef]
38. Teves, J.; Sola, E.F.; Pintor, B.H.; Ang, M.R.C. Assessing the Urban Solar Energy Resource Potential of Davao City, Philippines, using LiDAR Digital Surface Model (DSM) and GRASS GIS. In Proceedings of the Proceedings Volume 10008, Remote Sensing Technologies and Applications in Urban Environments, Edinburgh, UK, 26 October 2016; p. 1000809. [CrossRef]
39. Fu, P.; Rich, P.M. Design and implementation of the Solar Analyst: An ArcView extension for modeling solar radiation at landscape scales. In Proceedings of the 19th Annual ESRI User Conference, San Diego, CA, USA, 26–30 July 1999. Available online: https://proceedings.esri.com/library/userconf/proc99/proceed/papers/pap867/p867.htm (accessed on 9 September 2024).
40. Duffie, J.A.; Beckman, W.A.; Blair, N. *Solar Engineering of Thermal Processes. Photovoltaics and Wind*, 5th ed.; John Wiley & Sons: Hoboken, NJ, USA, 2020.

41. Iqbal, M. *An Introduction to Solar Radiation*; Academic Press Canada: Don Mills, ON, Canada, 1983.
42. Wald, L. *Basics in Solar Radiation at Earth Surface—Revised Version*; MINES ParisTech: Paris, France, 2019. Available online: https://minesparis-psl.hal.science/hal-02164311 (accessed on 9 September 2024).
43. Muneer, T. *Solar Radiation and Daylight Models*; Elsevier Butterworth-Heinemann: Oxford, UK, 2004.
44. World Radiation Centre. Available online: https://www.pmodwrc.ch/en/home/ (accessed on 10 August 2024).
45. Goswami, Y.; Kreith, F.; Kreider, J.F. *Principles of Solar Engineering*; Taylor & Francis: Philadelphia, PE, USA, 1999.
46. Kasten, F.; Young, A.T. Revised optical air mass tables and approximation formula. *Appl. Opt.* **1989**, *28*, 4735–4738. [CrossRef]
47. Cebecauer, T.; Huld, T.A.; Šúri, M. High resolution digital elevation model for improved PV yield estimates. In Proceedings of the 22nd European Photovoltaic Solar Energy Conference, Milano, Italy, 3–7 September 2007; pp. 3553–3557. Available online: https://publications.jrc.ec.europa.eu/repository/handle/JRC36425 (accessed on 9 September 2024).
48. JAXA. ALOS Global Digital Surface Model. Available online: https://www.eorc.jaxa.jp/ALOS/en/dataset/aw3d30/aw3d30_e.htm (accessed on 10 August 2024).
49. Alves, M.; Sanches, L.; Nogueira, J.; Silva, V. Effects of Sky Conditions Measured by the Clearness Index on the Estimation of Solar Radiation Using a Digital Elevation Model. *Atmos. Clim. Sci.* **2013**, *3*, 618–626. [CrossRef]
50. Liu, B.Y.H.; Jordan, R.C. The interrelationship and characteristic distribution of direct, diffuse and total solar radiation. *Sol. Energy* **1960**, *4*, 1–19. [CrossRef]
51. Mora-López, L.; Piliougine, M.; Carretero, J.E.; Sidrach-de-Cardona, M. Integration of Statistical and Machine Learning Models for Short-term Forecasting of the Atmospheric Clearness Index. In Proceedings of the 5th International Congress on Environmental Modelling and Sorftware, Ottawa, ON, Canada, 1 July 2010. Available online: https://scholarsarchive.byu.edu/iemssconference/2010/all/506/ (accessed on 6 September 2024).
52. Singh, J.; Bhattacharya, B.K.; Kumar, M.; Mallick, K. Modelling monthly diffuse solar radiation fraction and its validity over the Indian sub-tropics. *Int. J. Climatol.* **2013**, *33*, 77–86. [CrossRef]
53. Meteonorm. *METEONORM Global Meteorological Database. Handbook Part II. Theory*; IGI Global: Hershey, PA, USA, 2012.
54. Perez, R.; Ineichen, P.; Seals, R.; Michalsky, J.; Stewart, R. Modeling daylight availability and irradiance components from direct and global irradiance. *Sol. Energy* **1990**, *44*, 271–289. [CrossRef]
55. MMeehl, G.A.; Stocker, T.F.; Collins, W.D.; Friedlingstein, P.; Gaye, A.T.; Gregory, J.M.; Kitoh, A.; Knutti, R.; Murphy, J.M.; Noda, A.; et al. Global Climate Projections. In *Climate Change 2007: The Physical Science Basis. Contribution of Working Group I to the Fourth Assessment Report of the Intergovernmental Panel on Climate Change*; Solomon, S.D., Qin, M., Manning, Z., Chen, M., Marquis, K.B., Averyt, Tignor, M., Miller, H.L., Eds.; Cambridge University Press: Cambridge, UK; New York, NY, USA, 2007.
56. ESRI. ArcGIS Desktop. ArcMap. Points Solar Radiation. Available online: https://desktop.arcgis.com/en/arcmap/latest/tools/spatial-analyst-toolbox/points-solar-radiation.htm (accessed on 10 August 2024).